



Full length article

Effects of titanium and boron alloying with non-equimolar AlCrNbSiTi high entropy alloy nitride coatings



Igamcha Moirangthem ^{a,b}, Chaur-Jeng Wang ^a, Bih-Show Lou ^{c,d}, Ismail Rahmadtuloh ^{a,b}, Krishnakant Tiwari ^{b,e}, Jyh-Wei Lee ^{b,f,g,h,*}

^a Department of Mechanical Engineering, National Taiwan University of Science and Technology, Taipei, Taiwan

^b Department of Materials Engineering, Ming Chi University of Technology, New Taipei, Taiwan

^c Chemistry Division, Center for General Education, Chang Gung University, Taoyuan, Taiwan

^d Department of Orthopaedic Surgery, New Taipei Municipal TuCheng Hospital, Chang Gung Memorial Hospital, Taoyuan, Taiwan

^e Department of Materials Science and Engineering, National Taiwan University of Science and Technology, Taipei, Taiwan

^f Center for Plasma and Thin Film Technologies, Ming Chi University of Technology, New Taipei, Taiwan

^g College of Engineering, Chang Gung University, Taoyuan, Taiwan

^h High Entropy Materials Center, National Tsing Hua University, Hsinchu, Taiwan

ARTICLE INFO

Keywords:

Superimposed HiPIMS-MF

AlCrNbSiTiN

TiB₂

High entropy alloy coatings

Nanoindentation

ABSTRACT

Among various fabrication technologies for high entropy alloy coatings, high power impulse magnetron sputtering (HiPIMS) technologies have been utilized to synthesize dense microstructure and high hardness coatings with enhanced mechanical and chemical properties. Mid-frequency (MF) pulses have been introduced in the off-time of HiPIMS pulses of the superimposed HiPIMS-MF system to improve the deposition rate. In this study, AlCrNbSiTiBN coatings were deposited using a superimposed HiPIMS-MF system connected to an Al₄Cr₂NbSiTi₂ high entropy alloy target and a direct current (DC) power source for TiB₂ target in a reactive Ar and N₂ gas mixture. The DC power of the TiB₂ target was varied to increase the titanium and boron contents. With increasing Ti and B contents, the microstructure transforms from loose granular and crystalline structure to denser and refined nanocrystalline phases. A residual stress-free coating with a B content of 4.2 at.% and a hardness of 16.2 GPa was achieved without intentional heating and substrate bias. The poor corrosion resistance of the coatings with lower B contents can be enhanced with a further increase of B content up to 6.4 at.% and reaching a maximum of 10.3 times improvement than that of AISI 304 stainless steel.

1. Introduction

With the introduction of high entropy alloys [1] and multicomponent alloys [2] concepts, a new class of multi-principal element alloys different from conventional alloys has been a research focus due to their unique properties. In recent years, multi-principal element nitride coatings consisting of at least five principal elements have been found to perform high hardness [3,4], good wear resistance [5,6], oxidation resistance [7,8], and anticorrosion performance [9,10]. These coatings have been fabricated using various systems, including direct current magnetron sputtering (DCMS) [6,11], radio frequency magnetron sputtering (RFMS) [12,13], high power impulse magnetron sputtering (HiPIMS) [14,15], cathodic arc deposition (CAD) [16,17], arc ion plating [18], and vacuum arc spraying [19].

Transition binary and ternary metal nitride coatings have been widely considered for tribological applications due to their excellent mechanical properties such as high hardness and good wear resistance. Titanium nitride is among the most utilized nitrides for its applications in various tool. The addition of Al into such nitride coatings can effectively increase the tool lifetime depending on the usage environment [20]. Further multicomponent alloying designs had been proposed in search of the quality coatings for various usage environments [21]. A recent study on ternary nitride alloy AlCrTiN coating fabricated using RF magnetron sputtering had a hardness of 11.1 GPa and it improved the mechanical properties of Al—Si alloy substrates [22]. Addition of Si and Nb can also lead to enhanced mechanical and oxidation resistance properties due to the formation of nanocomposite structures consisting of nanocrystals in an amorphous matrix and ability to reduce oxygen

* Corresponding author at: Department of Materials Engineering, Ming Chi University of Technology, New Taipei, Taiwan.

E-mail address: jefflee@mail.mcut.edu.tw (J.-W. Lee).

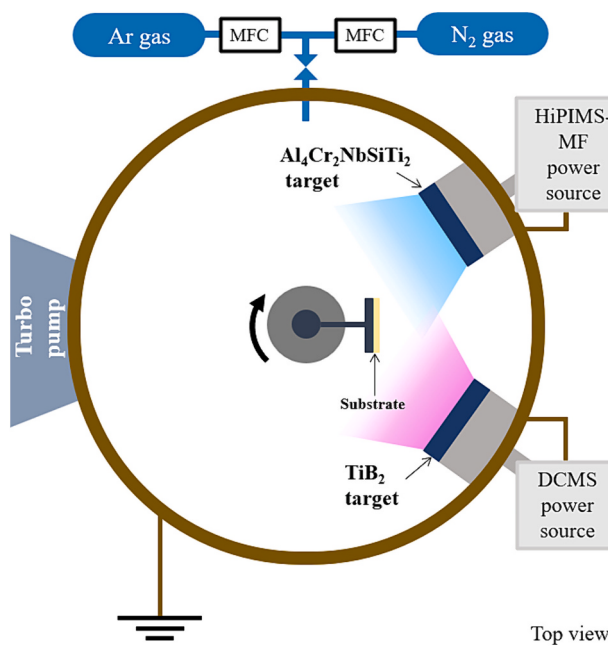


Fig. 1. Schematic diagram of the deposition system.

vacancies and slowing down oxygen diffusion [7,23].

Since the TiBN hard nitride coatings have been reported extensively in the literature because of their excellent hardness and wear resistant properties [24,25], addition of TiBN phase to multicomponent alloy nitride coating for enhancing their mechanical properties is a strategy to design the protective coatings. Superimposed high power impulse magnetron sputtering with mid-frequency (HiPIMS-MF) techniques have been utilized to fabricate various nitrides with a comparable or better mechanical properties with an enhanced deposition rate as compared to those of HiPIMS only [26,27]. Therefore, in this study we fabricated six AlCrNbSiTiBN coatings using a HiPIMS-MF and DCMS hybrid deposition system with varying titanium and boron contents and without intentional heating and substrate bias. Effects of Ti and B contents on the phase, microstructure, mechanical and anticorrosion properties of AlCrNbSiTiBN nitride coatings were discussed.

2. Experiments

2.1. Thin film depositions

A superimposed HiPIMS-MF power supply was connected to the

Al₄Cr₂NbSiTi₂ (HEA) target, and the TiB₂ target was supported by a DC power source. Five non-equimolar AlCrNbSiTiBN coatings with different titanium and boron contents were deposited on p-type Si (100) wafers, AISI 420, and 304 stainless steel (SS) substrates. The dimensions of the two rectangular targets were 304.8 × 127 × 6 mm. The superimposed HiPIMS and MF system (SIPP2000USB Dual, MELEC GmbH, Germany) consisted of two DC power sources, two separate 4000 μF capacitor banks, HiPIMS and MF pulse generating devices. The TiB₂ target was connected to the DC power supply for the reactive co-sputtering. One superimposed HiPIMS-MF cycle consisted of one HiPIMS pulse and twenty MF pulses. The duty cycle and repetition frequency of HiPIMS and MF were set at 2 %, 200 Hz and 50 %, 20,000 Hz, respectively. The pulse t_{on} and t_{off} of HiPIMS were fixed at 100 and 4900 μs (duty cycle of 2 %), respectively, while t_{on} and t_{off} of MF were set to be 25 μs for both (duty cycle of 50 %). The substrate holder was placed vertically parallel to the targets and rotated for 360° with a speed of 10 rpm, which made the substrates were in the plasma region for 1/3 of total deposition time and rotating out from the plasma region for the rest 2/3 deposition time. **Fig. 1** represents the schematics of the deposition system.

Prior to the deposition, Si wafers and SS substrates were cleaned with acetone and ethanol in ultrasonic cleaner. The substrates were then plasma etched for 15 min at a pressure of 1.07 Pa with an Ar gas flow rate of 50 sccm, and a DC substrate bias of -700 V. A Al₄Cr₂NbSiTi₂ HEA interlayer was deposited using HiPIMS power of 900 W at a pressure of 0.4 Pa under an Ar gas flow rate of 25 sccm, and a DC substrate bias of -100 V. The sample designations and detailed deposition parameters are listed in **Table 1**.

2.2. I-V and plasma characterization

The voltage and current of HEA target were measured during the deposition process using a digital oscilloscope (Keysight InfiniiVision DSO-X 2024A, Agilent Technologies, USA). The ion-eroded area of the HEA target, 200 cm², was used to calculate the peak power density of HiPIMS and MF power during deposition. An optical emission spectrometer (OES, PLASUS EMICON, Germany) was used to observe the difference in intensity of the neutral and ionic species present in the highest and the lowest peak power densities of the HiPIMS-MF plasma.

2.3. Sample characterization

The surface roughness of the thin films was examined by an atomic force microscope (AFM, DI-3100, Bruker, USA) in scan range of 5 × 5 μm². The surface and cross-sectional morphologies of films were characterized by a field emission scanning electron microscope (FE-SEM, JSM-6701, JEOL, Japan). The chemical composition analysis was

Table 1

Sample designation and deposition parameters of non-equimolar AlCrNbSiTiN with different titanium and boron contents coatings.

Sample designation	TB-0	TB-200	TB-300	TB-400	TB-500	TB-600
TiB ₂	DC power (W)	0	200	300	400	500
Al ₄ Cr ₂ NbSiTi ₂	HiPIMS	Power (W)	900	900	850	800
	Duty cycle (%)	2				
	Frequency (Hz)	200				
	On/Off time (μs)	100/4900				
	MF	Power (W)	900	900	850	800
	Duty cycle (%)	50				
	Frequency (Hz)	20,000				
	On/off time (μs)	25/25				
(Total MF pulse on-time/ HiPIMS on-time)/cycle	5					
Base pressure (Pa)		8 × 10 ⁻⁴				
Working pressure (Pa)		0.4				
N ₂ :Ar (sccm) [N ₂ flow rate ratio]		25:25 [50 %]				
Temperature		90 °C, No intentional heating				
Deposition time (min)		180				
Sample-target distance (cm)		14				
HEA interlayer		HiPIMS power = 900 W; bias: -100 V, thickness ~ 100 nm				

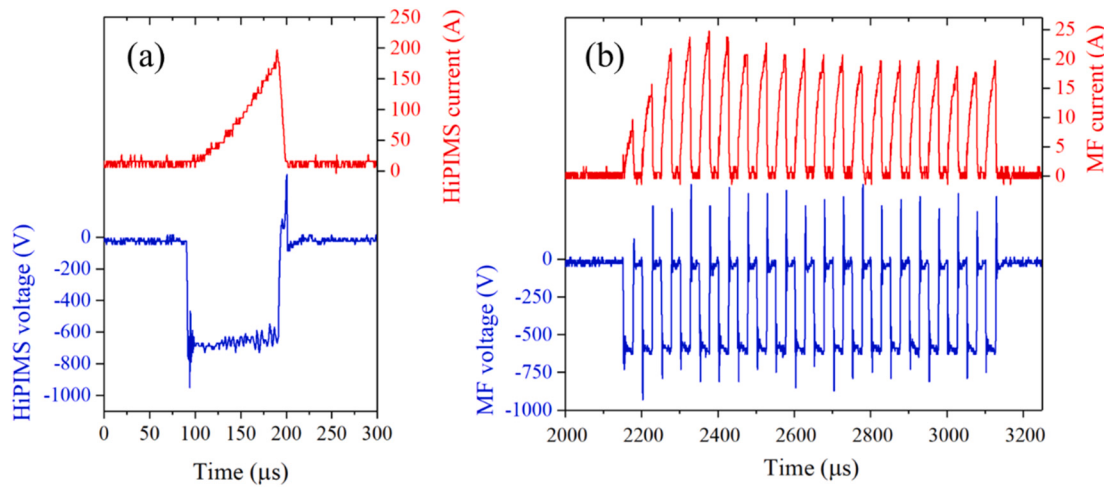


Fig. 2. Temporal evolutions of target voltage and current waveforms of HiPIMS and MF Al₄Cr₂NbSiTi₂ target during TB-0 deposition.

Table 2

I-V characteristics, voltage, peak current, and peak power density of HiPIMS and MF Al₄Cr₂NbSiTi₂ target.

Sample designation	TB-0	TB-200	TB-300	TB-400	TB-500	TB-600
HiPIMS	Voltage (V)	649	689	709	649	649
	Peak current (A)	197	187	166	166	156
	Peak power density (Wcm ⁻²)	639	644	588	539	506
MF	Voltage (V)	629	609	589	569	569
	Peak current (A)	25	26	24	22	20
	Peak power density (Wcm ⁻²)	78	78	70	61	56

carried out using a field emission electron probe microanalyzer (FE-EPMA, JXA-iHP200F, JEOL, Japan). The crystallography of each coating was evaluated by the thin film mode and powder mode in X-ray diffractometer (PANalytical, X'pert, Netherlands) using Cu K α radiation with an accelerating voltage of 45 kV, an emission current of 30 mA and omega of 1° in case of the grazing incidence mode.

The grain size, τ , of each thin film was calculated using Scherrer's equation [28] from the powder mode diffraction peaks,

$$\tau = \frac{0.9\lambda}{B \cos \theta_B}$$

where λ is the wavelength of the X-ray, B is the FWHM in radians, and θ_B is the Bragg angle.

The microstructures and phases of coatings were further observed using a transmission electron microscope (TEM, JEM-2100, JEOL, Japan). The hardness and elastic modulus were investigated using a nanoindenter (TI-950, TribolIndenter, Hysitron, USA) equipped with a Berkovich 142.3° diamond probe tip at a maximum displacement of 10 % of the total thickness of each coating. Eight indentation tests were performed for each sample. Using a general assumption of Poisson's ratio of 0.25 for ceramics, the elastic moduli (E) of AlCrNbSiTiN nitride coatings are calculated using the Oliver-Pharr method [29],

$$\frac{1}{E_r} = \frac{1 - \nu}{E} + \frac{1 - \nu_i}{E_i}$$

where E_r and ν are the reduced elastic modulus and Poisson's ratio of coating, respectively. The E_i of 1140 GPa and ν_i of 0.07 are the corresponding parameters of the diamond indenter.

The residual stresses of the coatings were measured using the laser curvature method in which the curvature of the Si substrate was measured before and after the deposition and calculated using Stoney's

equation [30],

$$\sigma = \frac{E_s}{6(1 - \nu_s)} \frac{h_s^2}{h_f} \left(\frac{1}{R} - \frac{1}{R_0} \right)$$

where E_s (= 130.2 GPa) is the Young's modulus, ν_s (= 0.279) is the Poisson's ratio, h_s (= 525 μ m) is the thickness of the Si substrate, h_f the thickness of the coating, R and R_0 are the curvature radii of the substrate after and before deposition.

Scratch test of coatings was performed using a conical diamond tip of radius 200 μ m, with an incremental normal load from 0.5 N to 75 N and a scratch length of 5 mm. A pin-on-disk wear method was used to investigate the tribological performance of the coatings. WC-6 wt% Co ball with 6 mm in diameter was adopted as a wear counterpart attached to the stationary pin. A normal load of 1 N was applied. The sliding speed was set to 10 cm/s with a wear track diameter of 6 mm. The wear length was kept at 50 m for each test to avoid the wear debris plowing into the substrate. Both scratch and wear tests were performed on the coatings fabricated on the 420SS substrates.

Potentiodynamic polarization tests in 3.5 wt% NaCl aqueous solution was carried out on the coatings deposited on 304SS substrates. The Ag-AgCl/KCl (saturated) with Luggin capillary and a Pt plate was used as the reference electrode and counter electrode, respectively. The scan range was set to 0.5 V below and 1.0 V above open circuit potential (OCP) with a scan rate of 1 mV/s. The potentiodynamic polarization experiment was stopped when the current density reached 1 mA/cm² to avoid excessive pitting corrosion on the coating.

3. Results and discussion

3.1. I-V characteristics

Fig. 2 represents the temporal evolution of target voltage and current waveform of HiPIMS and MF power during the deposition of TB-0 (similar temporal evolution for all cases). One HiPIMS-MF cycle is 5000 μ s consisting of a HiPIMS pulse width of 100 μ s (200 Hz frequency and 2 % duty cycle) and 20 MF pulses (MF cycle of 50 μ s, 20 kHz) with total width of 1000 μ s which is superimposed into the center of a HiPIMS off-time (4900 μ s) region. The setup of the superimposed HiPIMS-MF waveform can be seen in our previous study [26,27]. The increase of peak current up to the 5th MF pulse in **Fig. 2 (b)** and then decreasing to stable peak currents can be attributed to the discharge characteristics of the capacitor. **Table 2** gives a summary of the HiPIMS and MF voltages, peak current and peak power densities of the Al₄Cr₂NbSiTi₂ target during deposition. The highest peak power density of HiPIMS was 644 Wcm⁻² for TB-200, and the lowest for TB-600 was 474 Wcm⁻². The peak

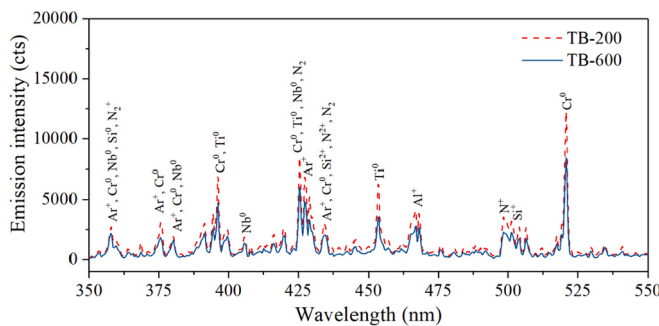


Fig. 3. OES spectra during sputtering of $\text{Al}_4\text{Cr}_2\text{NbSiTi}_2$ target during TB-200 and TB-600 depositions.

power density of MF was 78 Wcm^{-2} for TB-0 and TB-200 and dropped to 53 Wcm^{-2} for TB-600. The peak power densities of HiPIMS and MF gradually decrease in accordance with the decreasing setting average power. The increase in HiPIMS voltage from 649 V for TB-0 to 689 V for TB-200 and the decrease in peak current from 197 A (TB-0) to 187 A (TB-200) is due to the reduction in gas recycling [31] with the addition of reactive sputtering of TiB_2 target with DCMS power at the same total gas flow rate. The decrease in HiPIMS and MF voltage and peak current from TB-300 to TB-400 can be accounted for by the decrease in the average setting power of the target. Further, decrease in average setting power from TB-300 to TB-400 and so on leads to reduction only in peak current

while maintaining the same HiPIMS and MF voltage values.

3.2. Plasma emission characteristics

The optical emission spectrum of the HiPIMS-MF plasma of the $\text{Al}_4\text{Cr}_2\text{NbSiTi}_2$ target during TB-200 and TB-600 depositions is depicted in Fig. 3, which were obtained from the depositions with the highest and the lowest HiPIMS and MF peak power densities, respectively. Persistent emission peaks of the neutrals and ions, along with the overlapping peaks in the HiPIMS-MF plasma, are labeled according to emission line references [32]. Emission lines of Al^+ , Cr^0 , Nb^0 , Si^+ , Ti^0 , Ar^+ , and N^+ are observed at 466.3, 520.8, 405.6, 504.1, 453.4, 427.6, 499.4 nm, respectively. The highest emission line intensity was observed for Cr^0 with 12,268 counts for TB-200. An obvious intensity decrease of 31.2 % to 8445 counts for the Cr^0 line was observed as the set average target power of the $\text{Al}_4\text{Cr}_2\text{NbSiTi}_2$ target decreased from 1.8 kW for TB-200 to 1.4 kW for TB-600. A similar decrease in intensity for Al^+ and Ti^0 was observed, with 31.9 % and 43.4 % reduction, respectively. The measurement for the remaining emission lines was ignored due to the considerable overlapping of the neutral or ion emission lines. The decrease in average setting power from the highest set power of the HiPIMS-MF to the lowest results in a decrease of the emission line intensity but not the absence of the neutrals and ions, as observed in Fig. 3.

Table 3
Summary of properties of AlCrNbSiTiBN coatings.

Samples	TB-0	TB-200	TB-300	TB-400	TB-500	TB-600
TiB ₂ target power (W)	0	200	300	400	500	600
HEA HiPIMS power (W)	900	900	850	800	750	700
HEA MF power (W)	900	900	850	800	750	700
Composition						
Al	at.% Ratio	16.0 3.9	15.6 4.1	15.6 4.2	14.3 4.0	14.1 4.1
Cr	at.% Ratio	10.5 2.6	9.6 2.5	9.5 2.6	8.9 2.5	8.5 2.5
Nb	at.% Ratio	4.1 1.0	3.8 1.0	3.7 1.0	3.6 1.0	3.4 1.0
Si	at.% Ratio	4.8 1.2	4.7 1.2	4.5 1.2	4.3 1.2	4.2 1.2
Ti	at.% Ratio	10.4 2.5	10.0 2.6	10.3 2.8	10.3 2.9	10.5 3.1
B	at.% Ratio	— —	2.5 0.7	3.1 0.8	4.2 1.2	4.9 1.4
N	at.% Ratio	49.6 12.1	50.3 13.2	49.1 13.3	50.3 14.0	50.2 14.8
O	at.%	4.6	3.5	4.2	4.1	4.2
ΔS_{mix}		1.5 R	1.5 R	1.5 R	1.4 R	1.4 R
(Ti + B)/(Al + Cr + Nb + Si) ratio	0.29	0.37	0.40	0.47	0.51	0.58
Grain size (nm)	(111) (200)	54.4	48.2	42.9	36.6	33.7
Texture coefficient	(111) (200)	1.0 0.0	1.0 0.0	1.0 0.0	0.9 0.1	0.6 0.4
Lattice constant (\AA)	4.194	4.189	4.185	4.184	4.181	4.143
Thickness (nm)	1062	1090	1045	1044	939	854
Deposition rate (nm/min)	± 3	± 8	± 6	± 12	± 8	± 3
Hardness (GPa)	5.9	6.1	5.8	5.8	5.2	4.7
Elastic modulus (GPa)	9.3	12.0	13.5	16.2	15.4	13.0
H/E	± 1.0	± 0.7	± 0.7	± 1.1	± 1.5	± 0.5
H^3/E^2 (GPa)	182	199	200	205	198	181
Residual stress (GPa)	0.05	0.06	0.07	0.08	0.08	0.07
COF (μ)	0.02	0.04	0.06	0.10	0.09	0.07
Roughness, Ra (nm)	0.59	0.67	0.65	0.63	0.70	0.68
Wear rate, W_R [$\times 10^{-6}$] ($\text{mm}^3 \text{N}^{-1} \text{m}^{-1}$)	2.5	2.7	2.6	2.0	1.9	0.70
Average wear width (μm)	± 0.1	± 0.3	± 0.1	± 0.2	± 0.1	± 0.1
Average wear depth (μm)	6.2	9.8	12.0	11.0	18.0	14.0

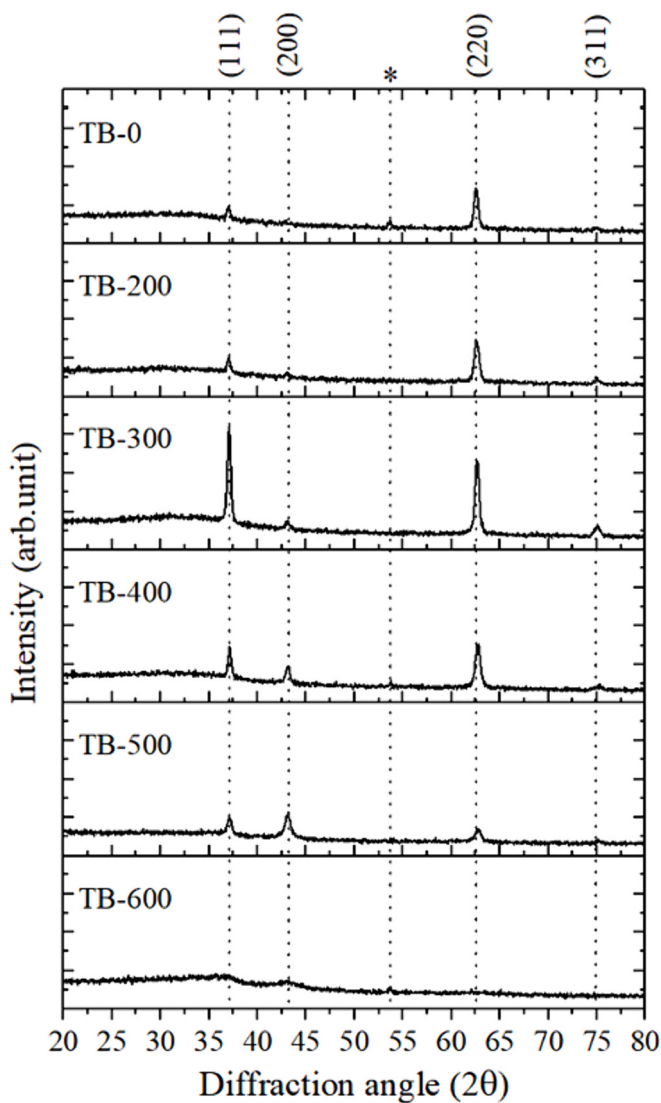


Fig. 4. Grazing incidence XRD patterns of the AlCrNbSiTiBN coatings.

3.3. Chemical compositions analysis

The atomic concentrations of the constituent elements and their ratios normalized to Nb atomic percent of the coatings are presented in [Table 3](#). Al, Cr, Nb, and Si concentrations show a decreasing trend with the decrease in HiPIMS-MF setting power. The $(\text{Ti} + \text{B})/(\text{Al} + \text{Cr} + \text{Nb} + \text{Si})$ ratio (named as TB ratio thereafter) increases from 0.29 to 0.58 as the TiB_2 target power increases from 0 to 600 W. Ti concentration is maintained at a similar concentration value ~ 10.4 to 10.7 at.% with the addition of Ti and B constituents. B content increases from 2.5 at.% for TB-200 to the highest of 6.4 at.% for TB-600 with increasing TiB_2 DCMS power. The nitrogen content varies between 49.1 at.% to 50.3 at.% for B content lower than 5 at.%, suggesting nitrogen saturation ~ 50 at.% for a 50 % N_2 flow rate ratio, similar to the reported literature [7]. But as the B content further increases, the nitrogen saturation increases to 52.2 at.%, which was similarly observed for B content multicomponent nitride [33]. The B in this deposition setup could easily form amorphous (a-BN) and hexagonal boron nitride (h-BN).

3.4. Microstructure and surface morphology

[Figs. 4 and 5](#) represent the grazing incidence and $0\text{-}2\theta$ scan X-ray diffraction patterns at selected FCC (111,200,220,222) plane regions of the coatings, respectively. As presented in [Fig. 4](#), the crystalline FCC phase in TB-0 and TB-200 were very similar. With increasing B content, the crystalline phase in TB-0 gradually transforms to a highly nanocrystalline phase, as in TB-500 and TB-600. The (111) reflection plane is energetically favorable in the absence of substrate bias. It is noticed that no TiB_2 phase can be seen, possibly due to its structure decomposition when it is mixed with these elements from the HEA target and nitrogen atoms. As a result, we can observe a preferred orientation of (111) in such grown films in the $0\text{-}2\theta$ scan, which is indicated by the texture coefficients in [Table 3](#). As the TiB_2 power increases, the Ti ratio and nitrogen content increase, and the lattice parameter has a decreasing tendency from the highest of 4.194 \AA to 4.143 \AA . The Nb atoms (empirical atomic radius, $r = 1.45 \text{ \AA}$) are increasingly substituted with smaller Ti atoms ($r = 1.40 \text{ \AA}$) in the disordered lattice. And the sudden decrease of the lattice parameter from 4.181 \AA in TB-500 to 4.143 \AA in TB-600 is due to the incorporation of more nitrogen as the sample becomes saturated. A small peak at 53.8° is unknown.

The surface and cross-sectional morphologies of six coatings are shown in [Fig. 6](#). TB-0 shows a loose granular surface feature, which is commonly seen in coatings deposited using DCMS and RFMS at low temperatures and without bias. This corresponds to the short duration exposure to the HiPIMS-MF plasma during the deposition process as

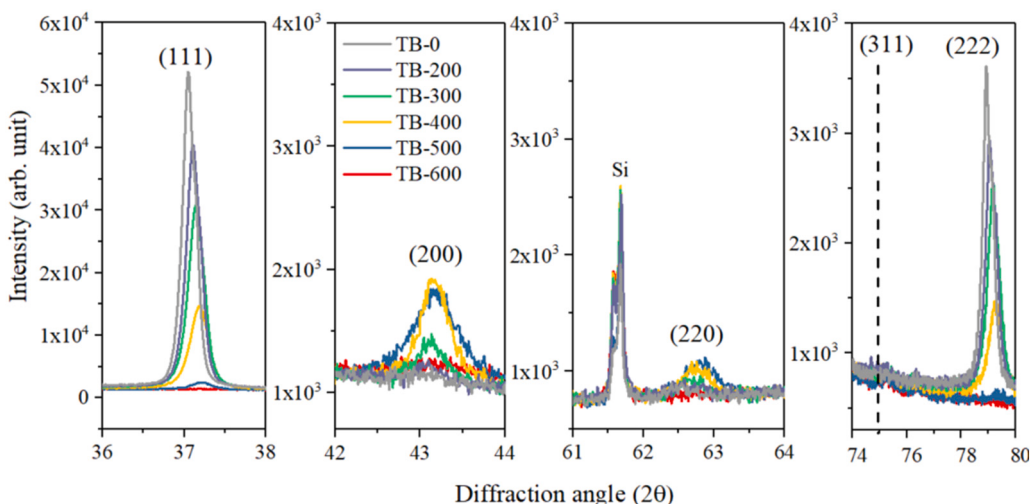


Fig. 5. Selected enlarged sections of $0\text{-}2\theta$ XRD patterns of the AlCrNbSiTiBN coatings.

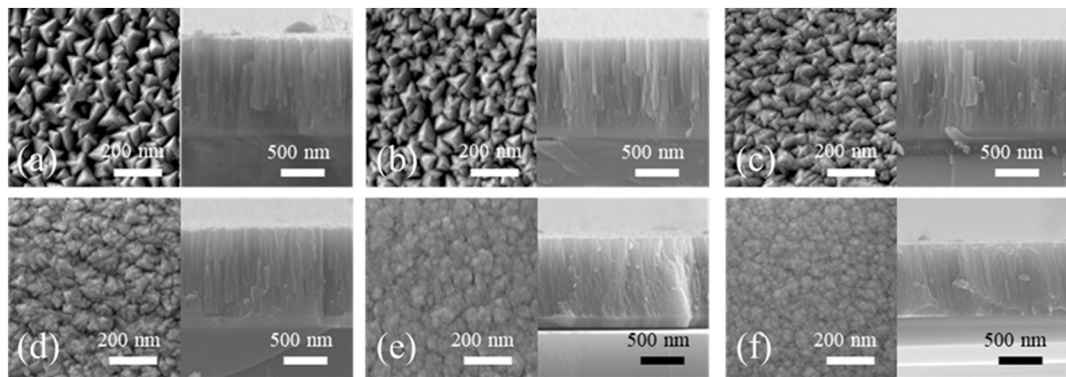


Fig. 6. Surface and cross-sectional FESEM images of (a) TB-0, (b) TB-200, (c) TB-300, (d) TB-400, (e) TB-500 and (f) TB-600.

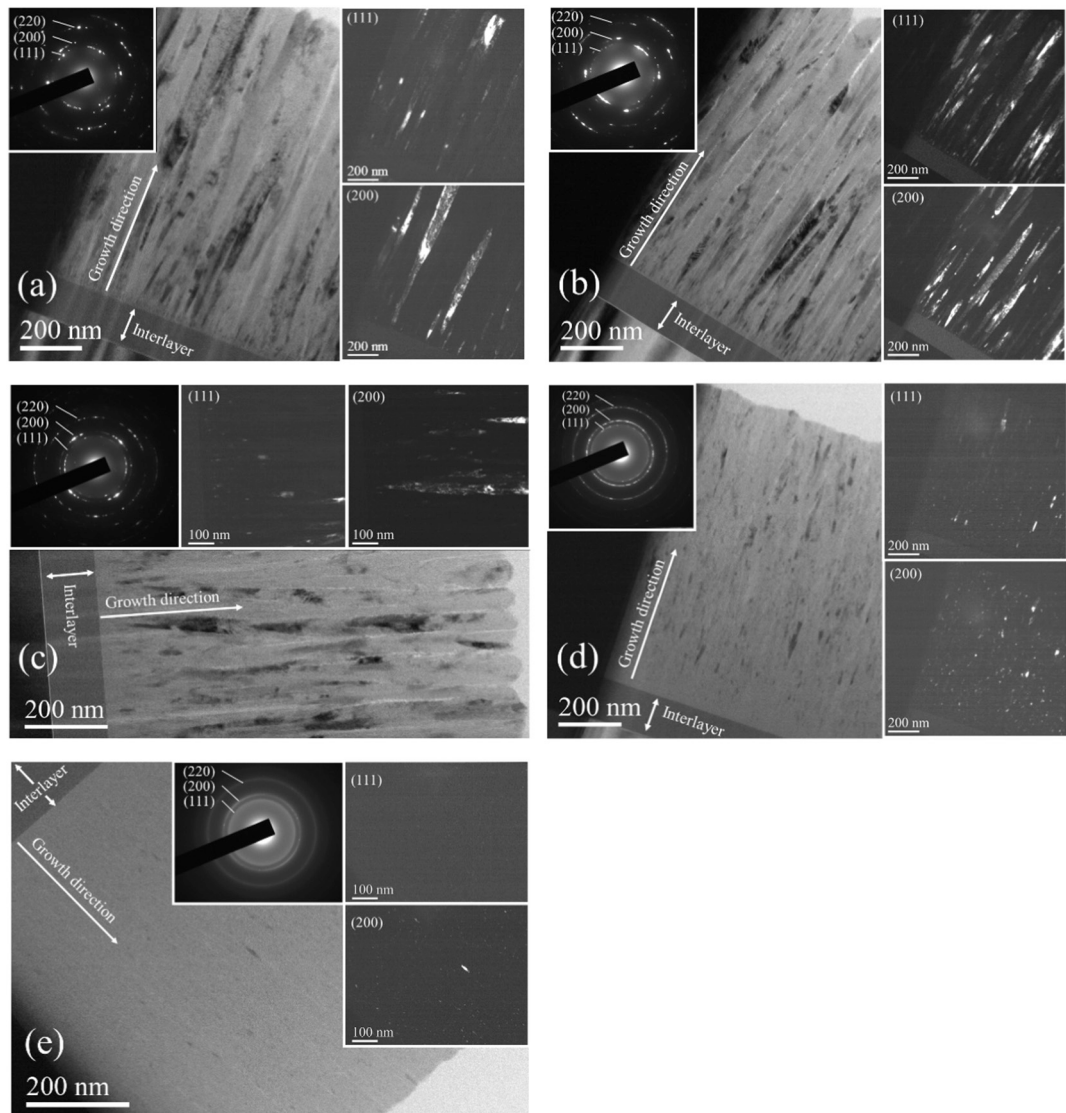


Fig. 7. TEM diffraction pattern, bright field, and dark field images of (a) TB-200, (b) TB-300, (c) TB-400, (d) TB-500, and (e) TB-600.

described above. The surface morphology gradually changes from loose granular to denser granular features as the TB ratio increases from 0.37 in TB-200 to 0.58 in TB-600. The decrease in granular surface feature is due to the grain refining effect induced by the addition of various nitride phases, such as amorphous BN, resulting from the reactive sputtering of

TiB₂, which leads to the formation of highly nanocrystalline phases in TB-600. The cross-sectional morphologies also follow a similar trend, gradually transitioning from loose columnar to slightly denser features as the TB ratio increases. The measured thickness and deposition rate of the coatings are presented in Table 3. The deposition rate slightly

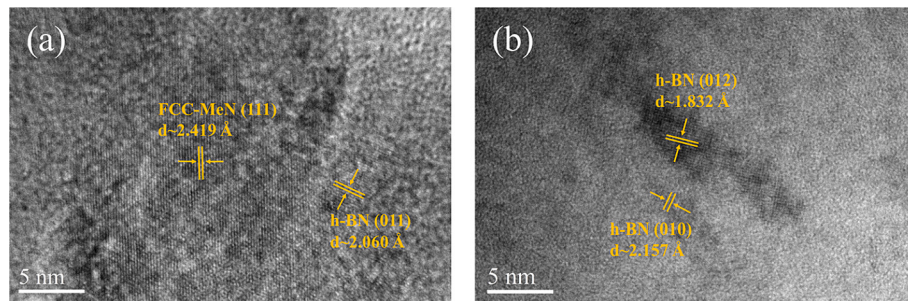
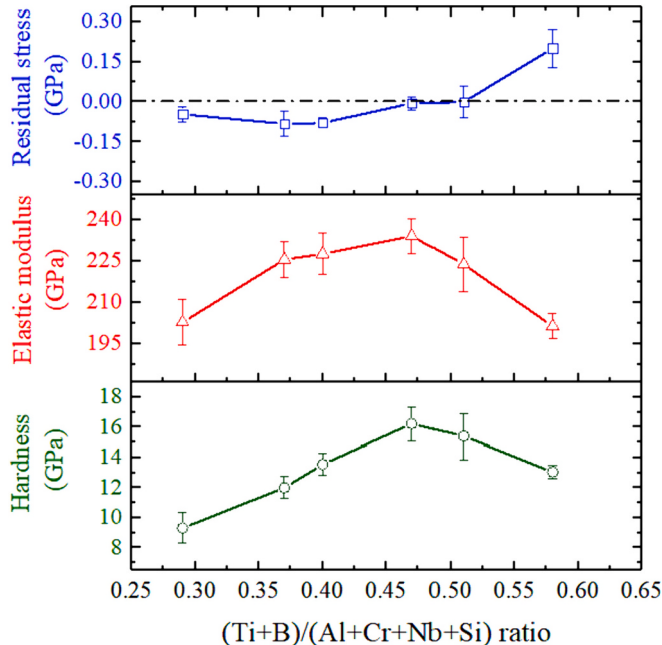
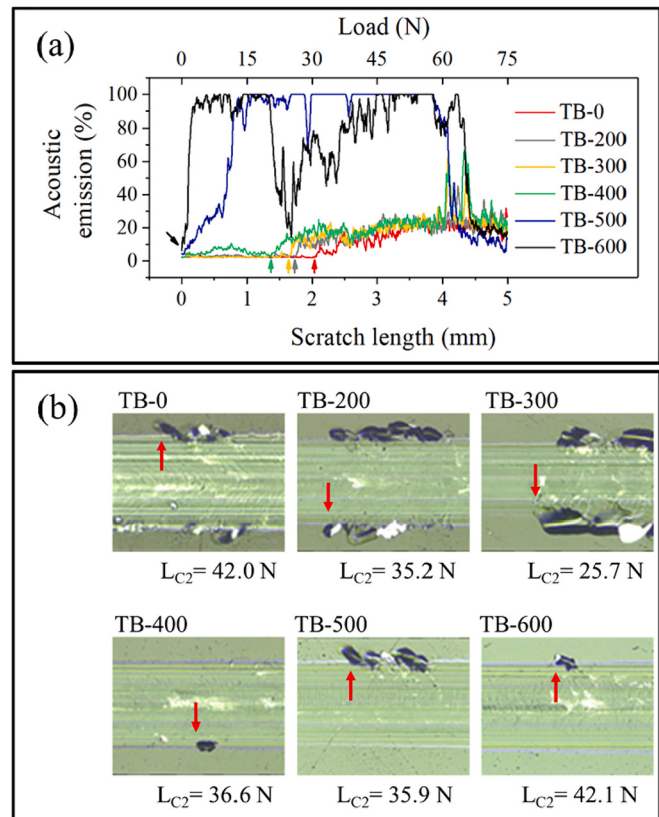


Fig. 8. High-resolution TEM images of (a) TB-500 and (b) TB-600.

Fig. 9. Hardness, elastic modulus, and residual stress versus $(\text{Ti} + \text{B})/(\text{Al} + \text{Cr} + \text{Nb} + \text{Si})$ ratio of the AlCrNbSiTiBN coatings.

increases from 5.9 nm/min for TB-0 to 6.1 nm/min for TB-200 due to reactive TiB_2 co-sputtering at first. It then gradually decreases with decreasing HEA average target power, reaching a minimum of 4.7 nm/min for TB-600. The average surface roughness values (R_a) of the coatings are presented in Table 3. The R_a value increases slightly from 2.5 nm in TB-0 to 2.7 nm in TB-200 with the addition of TiB_2 DCMS plasma and then gradually decreases to the lowest of 0.7 nm with increasing TB ratio. This is due to the more pronounced grain refining effect, which forms more refined nanostructural grains with lower average roughness values.

Fig. 7 shows the transmission electron microscopy images consisting of selected area electron diffraction (SAED) patterns, bright field (BF), and dark field (DF) micrographs for samples TB-200 through TB-600. TB-200, TB-300, and TB-400 show porous microstructure with visible voids in the cross-section due to lower adatom mobility in the absence of constant ion bombardment during the deposition process. The SAED pattern indicates the transition from polycrystalline to highly nanocrystalline as B content increases. The average columnar width of TB-200, TB-300, and TB-400 coatings are 64.7 nm, 45.1 nm, and 41.1 nm, respectively. A sudden transition in grain size is observed after TB-400 as B content reaches 4.9 at.%. The average size of nanograins of TB-500 and TB-600 are 14.9 nm and 8.0 nm, respectively. The high-resolution TEM images of TB500 and TB-600 are depicted in Fig. 8. The FCC HEA nitride nanocrystals were surrounded by amorphous BN

Fig. 10. (a) Acoustic emission versus scratch length and applied load during scratch tests with arrows indicating L_{C1} initiation sites and (b) optical micrographs indicating L_{C2} morphology of the AlCrNbSiTiBN coatings.

(a-BN) and hexagonal BN (h-BN). In TB-500, h-BN with (011) and in TB-600 h-BN with (012,010) reflection planes can be observed.

3.5. Mechanical properties evaluation

The hardness, elastic modulus, and residual stress versus TB ratio of the coatings are illustrated in Fig. 9, and their values are summarized in Table 3. The hardness increases from 9.3 GPa to the highest 16.2 GPa as the TB ratio reaches 0.47 in TB-400 due to the grain refinement effect. TB-400 can be considered to possess an optimum hardness for this batch as the hardness then decreases further to a lower value of 13.0 GPa in TB-600 with an increasing TB ratio; the decrease in hardness can be explained by the inverse Hall-Petch effect [34]. Even though the elastic moduli of the coatings follow a similar increasing and decreasing trend with the hardness, the values for TB-200 through TB-500 were within a similar range. The highest elastic modulus of 205 GPa can be observed for TB-400, and the lowest of 181 GPa is obtained for TB-600, which is

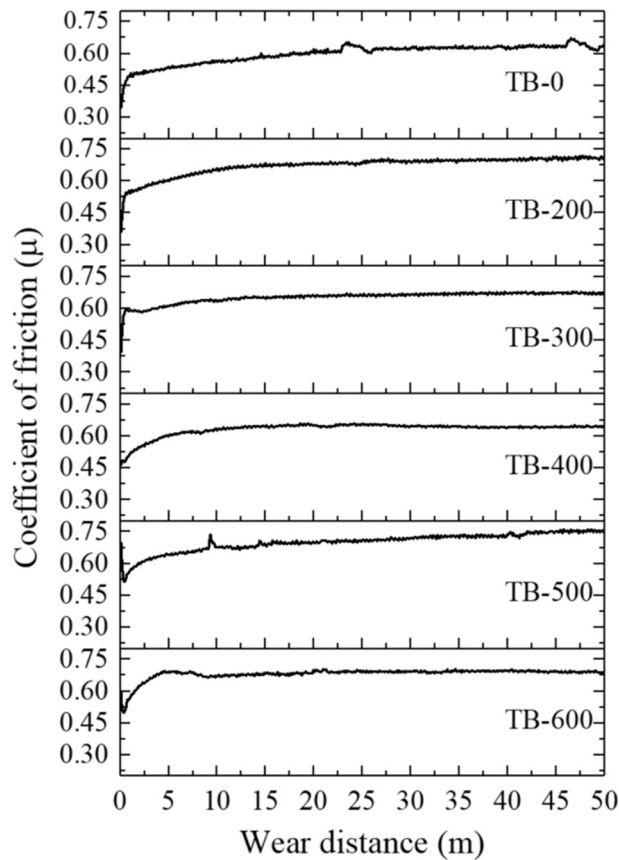


Fig. 11. Coefficient of friction versus wear distance of the AlCrNbSi-TiBN coatings.

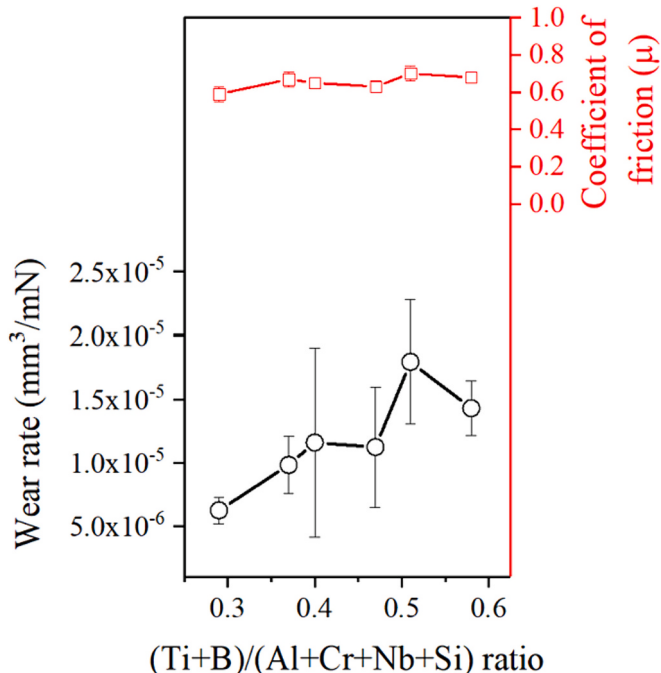


Fig. 12. Wear-rate and coefficient of friction values versus $(\text{Ti} + \text{B})/(\text{Al} + \text{Cr} + \text{Nb} + \text{Si})$.

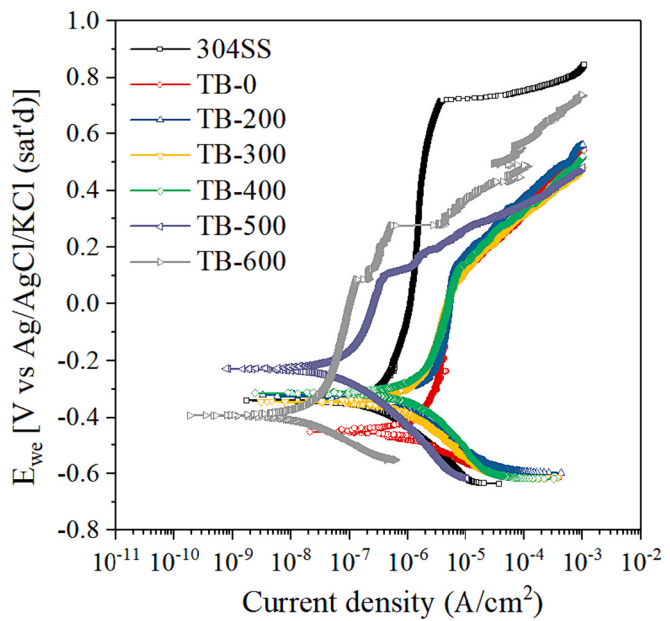


Fig. 13. Potentiodynamic polarization curve of the AlCrNbSiTiBN coatings.

quite similar to TB-0. The addition of Ti and B can result in the morphology transition from crystalline to nanocrystalline and also enhances the hardness slightly while maintaining a lower elastic modulus in TB-600. The lower hardness of these coatings in this work is due to the samples being out of the plasma region during 2/3 deposition duration time because of the 360° rotation of substrates as indicated in the experimental procedure. This leads to the absence of ion bombardment energy from the HiPIMS-MF and DCMS plasma when the samples were out of the plasma region, thus reducing surface adatom mobility, which negatively influences the quality of the coatings. Generally, higher adatom mobility due to constant ion-bombardment leads to defect-free development of the coatings by grain boundary migration and disallowing grain growth on the side facets. The development of porous cross-sectional microstructure due to lower adatom mobility is evident from the TEM cross-section images. A similar lower hardness value of 12 GPa was reported in the deposition of AlCrNbSiTiN HEA coating using the 360° substrate rotation method in our previous work [35].

The residual stresses of the coatings were all very low, which are ranging from -0.08 GPa (compressive nature) for TB-200 to 0.20 GPa (tensile nature) for TB-600 as TB ratio reaches 0.58. The substrate temperature gradually reaches up to only 90°C during all depositions, without any intentional heating, just from ion-bombardment from the HiPIMS-MF and DCMS plasma. This contributes to the lower thermal expansion during the deposition and lower residual stress in the coatings while maintaining higher hardness than the nitride-only coating, TB-0. The slight transition to tensile in TB-600 is due to the contraction of the lattice as the coating consists of more nanocrystals and h-BN phases, which have lower lattice parameters compared to an average of those of AlN, CrN, NbN, and TiN phases.

Fig. 10 (a) represents the acoustic emission signals during the scratch test versus scratch load and distance. The acoustic emission signal enables the precisely locating of the initiation of cohesive failures (L_{C1}) of the coatings as compared with the identification using an optical micrograph. The highest L_{C1} value among the coating was 30.7 N for TB-0. The L_{C1} values gradually decrease with increasing TB ratio. TB-500 and TB-600 show immediate cohesive failure with the initial application of 0.5 N scratch load. The L_{C1} failure locations are indicated accordingly with arrow marks in Figs. 10 (a) and (b). The poor cohesion performance arising from adding the Ti and B elements could be due to weak cohesive interactions among the crystals and increased h-BN content due to its poor wettability towards metal ceramics [36]. Fig. 10

Table 4

Potentiodynamic polarization values of AlCrNbSiTiBN coatings and AISI304 substrate.

Samples	AISI 304SS	TB-0	TB-200	TB-300	TB-400	TB-500	TB-600
(Ti + B)/(Al + Cr + Nb + Si) ratio	–	0.29	0.37	0.40	0.47	0.51	0.58
E_{corr} (mV)	−354.4	−448.5	−331.4	−344.0	−313.2	−228.6	−392.2
I_{corr} ($\mu A/cm^2$)	0.29	0.89	0.65	0.63	1.69	0.09	0.03
β_a (mV)	503.4	291.4	187.6	222.4	443.8	380.6	601.0
β_c (mV)	143.2	101.3	151.9	152.9	226.4	199.4	147.2
R_p (Ωcm^2) [$\times 10^6$]	0.17	0.04	0.06	0.06	0.04	0.63	1.71
R_p ratio	1	0.2	0.3	0.4	0.2	3.8	10.3

(b) shows the optical micrographs of L_{C2} failure points of the coatings. With reference to ASTM C1624-05 [37], the failure mode of the coatings can be classified as buckling spallation along with buckling cracks. The best L_{C3} was observed for TB-600 at 63.3 N owing to its dense nanocrystalline structure. The rest of the coatings had L_{C3} values lesser than 60 N.

The coefficient of friction (CoF) of the coatings plotted against the sliding distance is given in Fig. 11. The slight bumps in CoF of TB-0 at around 23 m and 46 m wear distance can be due to its rough surface and the formation of wear debris. The rest of the coatings show a relatively stable wear over the wear distance. The average CoF values are summarized in Table 3, and the CoF vs. TB ratio is given in Fig. 12. The lowest CoF of 0.59 can be seen for TB-0. With the addition of Ti and B elements, CoF slightly increases to 0.67 for TB-200 and then decreases to 0.63 for TB-400, following a similar increasing and decreasing trend of the roughness. A further increase of the TB ratio leads to an increase of CoF, as can be seen for TB-500 when its microstructure consists of more nanocrystals with very poor cohesion and the deposition regime dominated by DCMS plasma of the TiB₂ target as compared to TB-0 through TB-400. A slight decrease of CoF to 0.68 for TB-600 can be attributed to its lower roughness resulting from its nanocrystalline dense microstructure.

The wear rate versus TB ratio of the coatings is presented in Fig. 12. The lowest wear rate of $6.2 \times 10^{-6} mm^3/Nm$ is found for TB-0 despite its lower hardness and porous microstructure. The wear rate increases with the addition of Ti and B elements, reaching a maximum of $18.0 \times 10^{-6} mm^3/Nm$ for TB-500 with a TB ratio of 0.51. This is due to their declining L_{C1} value, as shown in Fig. 10, with increasing B content, which forms h-BN, leading to a lower cohesive force in the film than the nitride-only coating, TB-0. This implies that small h-BN content worsens the tribological performance by lowering the cohesion among the crystals/nanocrystals in the films. A slight improvement of the wear rate in TB-600 is due to its denser and pore free microstructure.

3.6. Corrosion resistance properties evaluation

Fig. 13 and Table 4 represent the potentiodynamic polarization results of the coatings. Tafel fit was used to obtain the polarization curve values. The corrosion resistances of TB-0, TB-200, TB-300, and TB-400 coatings were inferior to that of 304SS substrate due to their porous microstructures, which are shortcuts for electrolytes to attack the coatings. The constituent elements fail to form effective protective oxide films in such microstructures. As the porous columns become smaller and denser, the E_{corr} value becomes more positive. Without porous columns, the E_{corr} becomes more negative as the TB ratio increases from 0.51 in TB-500 to 0.58 in TB-600. Increasing B content leads to a more negative E_{corr} due to the presence of small metal boride phases [38]. The corrosion resistance is not improved until TB-500 and TB-600 where the coatings become a dense microstructure film and devoid of porous columns. When B content reaches 4.9 at.% in TB-500, the corrosion resistance improves drastically to an R_p ratio of 3.8. As the coating microstructure becomes more nanocrystalline in TB-600 (TB ratio of 0.58) with B content of 6.4 at.%, the best corrosion resistance among the coatings is observed with an R_p ratio of 10.3, which is due to its

comparatively dense microstructure resulted from its fine nanocrystalline grains embedded in the amorphous matrix in TB-600 to retard the penetration of corrosive electrolyte.

From the above analysis results, we can summarize that the effects on the AlCrNbSiTiBN coatings' quality are due to the amount of Ti and B in the form of (Ti + B)/(Al + Cr + Nb + Si) ratio. Ti is sputtered from both the HEA target and the TiB₂ target, so Ti content remains fairly similar, around 10.5 at.% in all coatings. The total effect can be expressed as the (Ti + B)/(Al + Cr + Nb + Si) ratio. Ti will likely occupy the disordered FCC lattice sites and reduce the lattice parameter as the Ti ratio increases in the film. The influence of B can be observed in the amorphization of the coatings. The lowest surface roughness and the best corrosion resistance can be seen for the coating containing the highest B of 6.4 at.% due to its amorphous microstructure.

4. Conclusion

In this study, a superimposed HiPIMS-MF deposition system was used to fabricate six AlCrNbSiTiBN coatings with varying Ti and B contents with (Ti + B)/(Al + Cr + Nb + Si) ratio (named as TB ratio) ranging from 0.29 to 0.58. Increasing TB ratio from 0.37 to 0.58 transformed the film microstructure from loose columnar crystalline to a denser and nanocrystalline structure. Without any intentional heating and substrate bias during deposition process, residual stress-free coating with the highest hardness of 16.2 GPa was obtained for the film with TB ratio of 0.47 whereas the lowest hardness of 9.3 GPa was observed for the B free coating. A smaller wear depth, wear width and the lowest wear rate of $6.2 \times 10^{-6} mm^3/Nm$ were obtained for TB-0 despite its lower hardness due to better film cohesion. The TB-600 coating containing 6.4 at.% B, with a TB ratio of 0.58, exhibited the highest corrosion resistance, which was 10.3 times better than AISI 304 stainless steel.

CRediT authorship contribution statement

Igamcha Moirangthem: Writing – original draft, Methodology, Investigation, Formal analysis, Data curation. **Chaur-Jeng Wang:** Supervision. **Bih-Show Lou:** Writing – review & editing, Validation, Resources, Funding acquisition. **Ismail Rahmadtulloh:** Investigation. **Krishnakant Tiwari:** Investigation. **Jyh-Wei Lee:** Writing – review & editing, Validation, Resources, Funding acquisition, Conceptualization.

Declaration of competing interest

The authors declare that they have no known competing financial interests or personal relationships that could have appeared to influence the work reported in this paper.

Acknowledgment

The authors would like to acknowledge funding from the National Science and Technology Council (NSTC) in Taiwan under Project Nos. NSTC 110-2221-E-131-004-MY3 and NSTC 112-2221-E-182-022. The financial support from the Chang Gung Memorial Hospital, Taiwan,

through Contract No. CMRPD5M0021 to B. S. Lou is also acknowledged. This work was also financially supported by the “High Entropy Materials Center” from The Featured Areas Research Center Program within the framework of the Higher Education Sprout Project by the Ministry of Education (MOE) in Taiwan.

References

- [1] J.-W. Yeh, S.-K. Chen, S.-J. Lin, J.-Y. Gan, T.-S. Chin, T.-T. Shun, C.-H. Tsau, S.-Y. Chang, Nanostructured high-entropy alloys with multiple principal elements: novel alloy design concepts and outcomes, *Adv. Eng. Mater.* 6 (2004) 299–303, <https://doi.org/10.1002/adem.200300567>.
- [2] B. Cantor, I.T.H. Chang, P. Knight, A.J.B. Vincent, Microstructural development in equiatomic multicomponent alloys, *Mater. Sci. Eng. A* 375–377 (2004) 213–218, <https://doi.org/10.1016/j.msea.2003.10.257>.
- [3] P.-K. Huang, J.-W. Yeh, Effects of nitrogen content on structure and mechanical properties of multi-element (AlCrNbSiTiN) coating, *Surf. Coat. Technol.* 203 (2009) 1891–1896, <https://doi.org/10.1016/j.surfcot.2009.01.016>.
- [4] S.-Y. Hsu, Y.-T. Lai, S.-Y. Chang, S.-Y. Tsai, J.-G. Duh, Combinatorial synthesis of reactively co-sputtered high entropy nitride (HFNBiTiVZrN) coatings: microstructure and mechanical properties, *Surf. Coat. Technol.* 442 (2022) 128564, <https://doi.org/10.1016/j.surfcot.2022.128564>.
- [5] P. Cui, W. Li, P. Liu, K. Zhang, F. Ma, X. Chen, R. Feng, P.K. Liaw, Effects of nitrogen content on microstructures and mechanical properties of (AlCrTiZrHf)N high-entropy alloy nitride films, *J. Alloys Compd.* 834 (2020) 155063, <https://doi.org/10.1016/j.jallcom.2020.155063>.
- [6] J. Wang, J. Fan, W. Li, P. Liu, X. Ma, K. Zhang, F. Ma, X. Chen, P.K. Liaw, Effects of nitrogen content on microstructures and mechanical behavior of (TiTaCrMoNb)N_x films, *Mater. Sci. Eng. A* 880 (2023) 145331, <https://doi.org/10.1016/j.msea.2023.145331>.
- [7] W.J. Shen, M.H. Tsai, K.Y. Tsai, C.C. Juan, C.W. Tsai, J.W. Yeh, Y.S. Chang, Superior oxidation resistance of (Al_{0.34}Cr_{0.22}Nb_{0.11}Si_{0.11}Ti_{0.22})₅₀N₅₀ high-entropy nitride, *J. Electrochem. Soc.* 160 (2013) C531, <https://doi.org/10.1149/2.028311jes>.
- [8] D.-C. Tsai, Z.-C. Chang, L.-Y. Kuo, T.-J. Lin, T.-N. Lin, M.-H. Shiao, F.-S. Shieh, Oxidation resistance and structural evolution of (TiVCrZrHf)N coatings, *Thin Solid Films* 544 (2013) 580–587, <https://doi.org/10.1016/j.tsf.2012.12.064>.
- [9] H.-T. Hsueh, W.-J. Shen, M.-H. Tsai, J.-W. Yeh, Effect of nitrogen content and substrate bias on mechanical and corrosion properties of high-entropy films (AlCrSiTiZr)_{100-x}N_x, *Surf. Coat. Technol.* 206 (2012) 4106–4112, <https://doi.org/10.1016/j.surfcot.2012.03.096>.
- [10] C. Zhang, X. Lu, H. Zhou, Y. Wang, X. Sui, Z. Shi, J. Hao, Construction of a compact nanocrystal structure for (CrNbTiAlVN) high-entropy nitride films to improve the tribo-corrosion performance, *Surf. Coat. Technol.* 429 (2022) 127921, <https://doi.org/10.1016/j.surfcot.2021.127921>.
- [11] T.H. Hsieh, C.H. Hsu, C.Y. Wu, J.Y. Kao, C.Y. Hsu, Effects of deposition parameters on the structure and mechanical properties of high-entropy alloy nitride films, *Curr. Appl. Phys.* 18 (2018) 512–518, <https://doi.org/10.1016/j.cap.2018.02.015>.
- [12] C.-H. Lai, S.-J. Lin, J.-W. Yeh, A. Davison, Effect of substrate bias on the structure and properties of multi-element (AlCrTaTiZr)N coatings, *J. Phys. D. Appl. Phys.* 39 (2006) 4628–4633, <https://doi.org/10.1088/0022-3727/39/21/019>.
- [13] J.-J. Wang, S.-Y. Chang, F.-Y. Ouyang, Effect of substrate bias on the microstructure and properties of (AlCrSiNbZr)N_x high entropy nitride thin film, *Surf. Coat. Technol.* 393 (2020) 125796, <https://doi.org/10.1016/j.surfcot.2020.125796>.
- [14] Y. Xu, G. Li, G. Li, F. Gao, Y. Xia, Effect of bias voltage on the growth of super-hard (AlCrTiVZr)N high-entropy alloy nitride films synthesized by high power impulse magnetron sputtering, *Appl. Surf. Sci.* 564 (2021) 150417, <https://doi.org/10.1016/j.apsusc.2021.150417>.
- [15] R. Shu, H. Du, G. Sadowski, M.M. Dorri, J. Rosen, M.A. Sortica, D. Premetzhofer, D. Lundin, A. le Febvrier, P. Eklund, Multicomponent Ti_xNbCrAl nitride films deposited by dc and high-power impulse magnetron sputtering, *Surf. Coat. Technol.* 426 (2021) 127743, <https://doi.org/10.1016/j.surfcot.2021.127743>.
- [16] A. Lothrop, Q. Yang, X. Huang, X. Wu, Characterization of (AlCrTiVZr)N high-entropy coating produced by cathodic arc evaporation, *J. Mater. Eng. Perform.* (2023), <https://doi.org/10.1007/s11665-023-08485-1>.
- [17] Y. Zhao, S. Chen, Y. Chen, S. Wu, W. Xie, W. Yan, S. Wang, B. Liao, S. Zhang, Superhard and anti-corrosion (AlCrMoSiTi)N_x high entropy nitride coatings by multi-arc cathodic vacuum magnetic filtration deposition, *Vacuum* 195 (2022) 110685, <https://doi.org/10.1016/j.vacuum.2021.110685>.
- [18] J. Liu, X. Zhang, X. Zeng, Z. Xiong, Y. Liu, Y. Lei, B. Yang, Effect of bias voltages on microstructure and mechanical properties of (AlCrNbSiTi)N high entropy alloy nitride coatings deposited by arc ion plating, *Surf. Eng.* 39 (2023) 495–505, <https://doi.org/10.1080/02670844.2023.2236829>.
- [19] V.F. Gorban, I.M. Zakiev, G.F. Sarzhan, Comparative friction characteristics of high-entropy mononitride coatings, *J. Frict. Wear* 37 (2016) 263–267, <https://doi.org/10.3103/S1068366616030077>.
- [20] O. Knotek, W.D. Münz, T. Leyendecker, Industrial deposition of binary, ternary, and quaternary nitrides of titanium, zirconium, and aluminum, *J. Vac. Sci. Technol. Vac. Surf. Films* 5 (1987) 2173–2179, <https://doi.org/10.1116/1.574948>.
- [21] H.A. Jehn, Multicomponent and multiphase hard coatings for tribological applications, *Surf. Coat. Technol.* 131 (2000) 433–440, [https://doi.org/10.1016/S0257-8972\(00\)00783-0](https://doi.org/10.1016/S0257-8972(00)00783-0).
- [22] F.A. Orjuela, F.F. Vallejo, H. Hahn, J.J. Olaya, J.E. Alfonso, L. Velasco, Nitrogen flux effect on the mechanical properties of AlCrTiN nanostructured coatings obtained by R. F. magnetron sputtering, *Ceram. Int.* 49 (2023) 17867–17875, <https://doi.org/10.1016/j.ceramint.2023.02.153>.
- [23] M.-H. Hsieh, M.-H. Tsai, W.-J. Shen, J.-W. Yeh, Structure and properties of two Al–Cr–Nb–Si–Ti high-entropy nitride coatings, *Surf. Coat. Technol.* 221 (2013) 118–123, <https://doi.org/10.1016/j.surfcot.2013.01.036>.
- [24] P.H. Mayrhofer, M. Stoiber, Thermal stability of superhard Ti–B–N coatings, *Surf. Coat. Technol.* 201 (2007) 6148–6153, <https://doi.org/10.1016/j.surfcot.2006.08.132>.
- [25] R. Hahn, A. Tymoszuk, T. Wojcik, A. Kirmbauer, T. Kozák, J. Čapek, M. Sauer, A. Foelske, O. Hunold, P. Polcik, P.H. Mayrhofer, H. Riedl, Phase formation and mechanical properties of reactively and non-reactively sputtered Ti-B-N hard coatings, *Surf. Coat. Technol.* 420 (2021) 127327, <https://doi.org/10.1016/j.surfcot.2021.127327>.
- [26] W. Diyatmika, F.-K. Liang, B.-S. Lou, J.-H. Lu, D.-E. Sun, J.-W. Lee, Superimposed high power impulse and middle frequency magnetron sputtering: role of pulse duration and average power of middle frequency, *Surf. Coat. Technol.* 352 (2018) 680–689, <https://doi.org/10.1016/j.surfcot.2017.11.057>.
- [27] B.-S. Lou, M. Annalakshmi, Y.-W. Su, W.-S. Yang, J.-W. Lee, Fabrication of TiN coatings using superimposed HiPIMS pulse on-time ratio, *Surf. Coat. Technol.* (2024) 130364, <https://doi.org/10.1016/j.surfcot.2023.130364>.
- [28] B.D. Cullity, S.R. Stock, *Elements of X-ray Diffraction, Third Edition*, 2014.
- [29] W.C. Oliver, G.M. Pharr, Measurement of hardness and elastic modulus by instrumented indentation: advances in understanding and refinements to methodology, *J. Mater. Res.* 19 (2004) 3–20, <https://doi.org/10.1557/jmr.2004.19.1.3>.
- [30] M.R. Ardigo, M. Ahmed, A. Besnard, Stoney formula: investigation of curvature measurements by optical profilometer, *Adv. Mater. Res.* 996 (2014) 361–366, <https://doi.org/10.4028/www.scientific.net/AMR.996.361>.
- [31] A. Anders, Tutorial: reactive high power impulse magnetron sputtering (R-HiPIMS), *J. Appl. Phys.* 121 (2017) 171101, <https://doi.org/10.1063/1.4978350>.
- [32] J.E. Sansonetti, W.C. Martin, Handbook of basic atomic spectroscopic data, *J. Phys. Chem. Ref. Data Monogr.* 34 (2005) 1559–2259, <https://doi.org/10.1063/1.1800011>.
- [33] C.-W. Tsai, S.-W. Lai, K.-H. Cheng, M.-H. Tsai, A. Davison, C.-H. Tsau, J.-W. Yeh, Strong amorphization of high-entropy AlBCrSiTi nitride film, *Thin Solid Films* 520 (2012) 2613–2618, <https://doi.org/10.1016/j.tsf.2011.11.025>.
- [34] A.H. Chokshi, A. Rosen, J. Karch, H. Gleiter, On the validity of the hall-petch relationship in nanocrystalline materials, *Scr. Metall.* 23 (1989) 1679–1683, [https://doi.org/10.1016/0036-9748\(89\)90342-6](https://doi.org/10.1016/0036-9748(89)90342-6).
- [35] B.-S. Lou, Y.-C. Lin, J.-W. Lee, Mechanical properties and corrosion resistance of AlCrNbSiTiN high entropy alloy nitride coatings, *Coatings* 13 (2023) 1724, <https://doi.org/10.3390/coatings13101724>.
- [36] J. Eichler, C. Lesniak, Boron nitride (BN) and BN composites for high-temperature applications, *J. Eur. Ceram. Soc.* 28 (2008) 1105–1109, <https://doi.org/10.1016/j.jeurceramsoc.2007.09.005>.
- [37] ASTM C1624-05, Test method for adhesion strength and mechanical failure modes of ceramic coatings by quantitative single point scratch testing, ASTM Int. (2015), <https://doi.org/10.1520/C1624-05R15>.
- [38] J. Guo, Z. Liu, Y. Su, Effect of B on microstructure and properties of surfacing layer of austenitic stainless steel flux cored wire, *Materials* 15 (2022) 5884, <https://doi.org/10.3390/ma15175884>.